International Journal of Solids and Structures 69–70 (2015) 71–85

Contents lists available at ScienceDirect

International Journal of Solids and Structures

journal homepage: www.elsevier.com/locate/ijsolstr

Instabilities in thin films on hyperelastic substrates by 3D finite elements

Fan Xu [a,b,*], Yao Koutsawa [b], Michel Potier-Ferry [a], Salim Belouettar [b]

[a] Laboratoire d'Etude des Microstructures et de Mécanique des Matériaux, LEM3, UMR CNRS 7239, Université de Lorraine, Ile du Saulcy, 57045 Metz Cedex 01, France
[b] Luxembourg Institute of Science and Technology (LIST), 5 avenue des Hauts-Fourneaux, L-4362 Esch-sur-Alzette, Luxembourg

ARTICLE INFO

Article history:
Received 12 February 2015
Received in revised form 22 April 2015
Available online 18 June 2015

Keywords:
Wrinkling
Post-buckling
Bifurcation
Neo-Hookean hyperelasticity
Path-following technique
Automatic Differentiation

ABSTRACT

Spatial pattern formation in thin films on rubberlike compliant substrates is investigated based on a fully nonlinear 3D finite element model, associating nonlinear shell formulation for the film and finite strain hyperelasticity for the substrate. The model incorporates Asymptotic Numerical Method (ANM) as a robust path-following technique to predict a sequence of secondary bifurcations on their post-buckling evolution path. Automatic Differentiation (AD) is employed to improve the ease of the ANM implementation through an operator overloading, which allows one to introduce various potential energy functions of hyperelasticity in quite a simple way. Typical post-buckling patterns include sinusoidal and checkerboard, with possible spatial modulations, localizations and boundary effects. The proposed finite element procedure allows accurately describing these bifurcation portraits by taking into account various finite strain hyperelastic laws from the quantitative standpoint. The occurrence and evolution of 3D instability modes including fold-like patterns will be highlighted. The need of finite strain modeling is also discussed according to the stiffness ratio of Young's modulus.

1. Introduction

Broad interests on surface morphological instabilities of stiff thin layers attached on soft substrates have motivated a large number of research studies over the last decade (Bowden et al., 1998; Efimenko et al., 2005; Rogers et al., 2010; Brau et al., 2011; Stoop et al., 2015). Several theoretical, numerical and experimental works have been devoted to stability analyses in order to determine the critical conditions of instability and the corresponding wrinkling patterns (Chen and Hutchinson, 2004; Huang et al., 2004, 2005; Huang and Im, 2006; Wang et al., 2008; Song et al., 2008; Audoly and Boudaoud, 2008a,b,c). In particular, there are several analytical solutions of models linearized from homogeneous finite deformation, in the case of half-spaces (Hayes and Rivlin, 1961; Dowaikh and Ogden, 1990; Shield et al., 1994) and film/substrate systems (Steigmann and Ogden, 1997; Cai and Fu, 1999, 2000). Although linear perturbation analyses can predict the wavelength at the initial stage of instability threshold, determination of the post-bifurcation response and the mode transition of surface wrinkles really requires nonlinear buckling analyses. During post-buckling, the wrinkle wavelength and amplitude will vary with respect to externally applied compressive load. Due to its well-known difficulty, most post-buckling analyses have resorted to numerical approaches since only a limited number of exact analytical solutions can be obtained in very simple or simplified cases.

Nevertheless, surface instability of stiff layers on soft materials usually involves strong geometrical nonlinearities, large rotations, large displacements, large deformations, loading path dependence, multiple symmetry-breakings, nonlinear constitutive relations, localizations and other complexities, which makes the numerical resolution quite difficult. The morphological post-buckling evolution and mode shape transition beyond the critical load are incredibly complicated, especially in 3D cases, and conventional numerical methods have difficulties in predicting the post-bifurcation response on their complex evolution paths. Reliable and robust numerical techniques are in strong demand for post-buckling response of film/substrate system, especially for predicting and tracing the surface mode transition.

In most of early studies, the 2D or 3D spatial problem of film/substrate is often discretized by either spectral method or Fast Fourier Transform (FFT) algorithm, which is fairly computationally inexpensive but prescribes periodic boundary conditions and simple geometries. Moreover, within the spectral or FFT framework, it is rather difficult to describe localized behavior that often occurs in soft matters such as folding, creasing and ridging. Recent efforts

* Corresponding author at: Laboratoire d'Etude des Microstructures et de Mécanique des Matériaux, LEM3, UMR CNRS 7239, Université de Lorraine, Ile du Saulcy, 57045 Metz Cedex 01, France.
E-mail address: fan.xu@univ-lorraine.fr (F. Xu).

http://dx.doi.org/10.1016/j.ijsolstr.2015.06.007
0020-7683/

have been devoted to 2D plane strain study of such localizations by using finite element methods (Cao and Hutchinson, 2012a,b; Cao et al., 2012; Sun et al., 2012; Zang et al., 2012; Xu et al., 2015), which is more computationally expensive but more flexible to describe complex geometries and general boundary conditions, and allows using commercial computer codes. Localizations are often caused by stress concentration due to the real boundary and loading conditions or by symmetry-breakings due to substrate nonlinearity, and finite element modeling is a good way to capture such localized behavior.

The previous works of Xu et al. (2014, 2015) propose a whole numerical framework to study surface wrinkling of thin films bound to soft substrates, through applying advanced numerical methods for bifurcation analyses to typical cases of film/substrate systems and focusing on the post-buckling evolution involving multiple bifurcations, for the first time addressing the post-bifurcation response of film/substrate systems from the quantitative standpoint. The stiff thin film undergoing moderately large deflections is described by either nonlinear shell formulation or Föppl–von Kármán nonlinear approximation, while the substrate is limited to be small strain linear elasticity. These assumptions make sense in the case of a large stiffness ratio E_f/E_s in the range $\mathcal{O}(10^4) \sim \mathcal{O}(10^5)$, E_f and E_s being Young's modulus of the film and the substrate, respectively. In this range, critical strains are very small and thus the linear elastic framework is relevant (Chen and Hutchinson, 2004). In this framework, the occurrence and post-buckling evolution of several typical 2D or 3D wrinkling modes like sinusoidal, checkerboard and herringbone were thoroughly investigated (Xu et al., 2014, 2015; Xu, 2014). Some recent studies consider much softer films made of polymeric materials (Brau et al., 2011; Cao and Hutchinson, 2012a; Yin et al., 2012), typically with a stiffness ratio E_f/E_s in the range $\mathcal{O}(1) \sim \mathcal{O}(10)$, where the critical strain could be relatively large in the substrate, especially in the vicinity of the interface and the small strain framework is no more appropriate. Moreover, some instability modes caused by symmetry-breakings require the nonlinearity of the substrate to be taken into account. Therefore, finite strain models such as neo-Hookean hyperelasticity should be considered for the substrate (Hutchinson, 2013). In this paper, hyperelastic substrates will be employed and the resulting responses will be compared with the assumption of linear elastic substrates that are chosen in many papers (Chen and Hutchinson, 2004; Audoly and Boudaoud, 2008a; Xu et al., 2014, 2015).

This paper aims at studying the occurrence and evolution of 3D instability patterns through applying advanced numerical methods. Spatial pattern formation of film/substrate is investigated based on a fully nonlinear 3D finite element model associating finite strain hyperelasticity for the substrate and geometrically nonlinear shell formulation for the film. The model incorporates Asymptotic Numerical Method (ANM) (Damil and Potier-Ferry, 1990; Cochelin et al., 1994, 2007; Cochelin, 1994) as a robust path-following technique to predict a sequence of secondary bifurcations on their post-buckling evolution path as the load is increased. The tracing of post-bifurcation response is an important and difficult numerical problem. The ANM gives interactive access to semi-analytical equilibrium branches, which offers considerable advantage of reliability compared with classical iterative algorithms. The underlying principle of the ANM is to build up the nonlinear solution branch in the form of relatively high order truncated power series. The resulting series are then introduced into the nonlinear problem, which helps to transform it into a sequence of linear problems that can be solved numerically. By taking the advantage of the local polynomial approximations of the branch within each step, the algorithm is remarkably robust and fully automatic. Furthermore, unlike incremental-iterative methods, the arc-length step size in the ANM is fully adaptive since it is determined *a posteriori* by the algorithm. A small radius of convergence and step accumulation appear around the bifurcation and imply its presence.

The implementation of the ANM can be cumbersome and not straightforward when dealing with some complex potential functions such as hyperelasticity (Nezamabadi et al., 2011) or discontinuous nanoscale problems (Cong et al., 2014). To facilitate the computing of the asymptotic coefficients of Taylor series, Automatic Differentiation (AD) techniques (Griewank, 2000) have been proposed to compute high order derivatives of constitutive laws (Koutsawa et al., 2008; Charpentier and Potier-Ferry, 2008; Lejeune et al., 2012, 2013). The AD techniques can significantly improve the ease of the ANM implementation through an operator overloading (Koutsawa et al., 2008; Charpentier and Potier-Ferry, 2008), which allows one to introduce various potential energy functions of hyperelastic laws in a rather simple and efficient manner.

This paper explores the occurrence and post-buckling evolution of 3D instability modes from the quantitative standpoint in greater depth. The paper is outlined as follows. In Section 2, a nonlinear 3D film/substrate model is developed, by accounting for finite strain hyperelasticity for the substrate. Then in Section 3, the resulting nonlinear problem is reformulated by the ANM algorithm as a perturbation technique and AD techniques are performed to facilitate the ANM implementation. Results and discussions are provided in Section 4, including the onset and evolution of folded modes under different loading and boundary conditions. Comparisons between finite strain models and linear elastic models with respect to different stiffness ranges of Young's modulus are investigated. Conclusions are reported in Section 5.

2. 3D model

We consider an elastic thin film bonded to a hyperelastic substrate, which can buckle under compression. Upon wrinkling, the film elastically buckles to relax the compressive stress and the substrate concurrently deforms to maintain perfect bonding at the interface. In the post-buckling stage, the film undergoes large rotations and large displacements but the strain can be small. In this case, it is reasonable to assume the film as linear elastic materials. Therefore, in the following, the elastic potential energy of the film is considered in the framework of Hookean elasticity. However, when the wrinkling amplitude is large, the strain of the substrate in the vicinity of the interface can be large. Recent studies have revealed that the nonlinearity of the substrate leads to symmetry-breakings and affects the mode shape when the slopes of the film increase (Li et al., 2011; Cao and Hutchinson, 2012a; Sun et al., 2012; Zang et al., 2012; Stoop et al., 2015). Hence, it is preferred to apply hyperelastic material formulations to deal with the substrate. Besides, in practice, the substrate made of rubberlike materials such as elastomers often undergoes finite deformations without tearing and with almost instantaneously recoverable strains. To model such rubberlike substrate, linear elasticity theory is no more appropriate and hyperelastic constitutive laws have to be considered.

The film/substrate system is considered to be three-dimensional and the geometry is as shown in Fig. 1. Let x and y be in-plane coordinates, while z is the direction perpendicular to the mean plane of the film/substrate. The width and length of the system are denoted by L_x and L_y, respectively. The parameters h_f, h_s and h_t represent, respectively, the thickness of the film, the substrate and the total thickness of the system. Young's modulus and Poisson's ratio of the film are respectively denoted by E_f and ν_f, while E_s and ν_s are the corresponding material properties for the substrate.

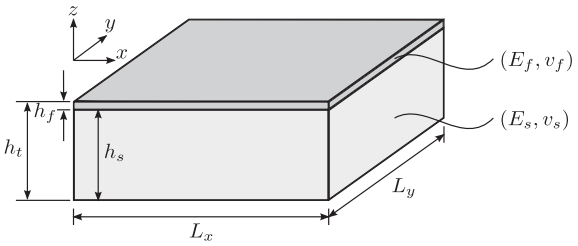

Fig. 1. Geometry of film/substrate system.

2.1. Nonlinear hyperelasticity for the substrate

Generally, the mechanical response of hyperelastic materials is described by strain energy potential function, Ψ, to fit the particular material. This function is a continuous scalar-valued function and is given in terms of the deformation gradient tensor, $\mathbf{F} = \nabla\mathbf{u} + \mathbf{I}$ ($\mathbf{u}$ being the displacement field and $\mathbf{I}$ being the second-order identity tensor), or some strain tensors, $\Psi = \Psi(\mathbf{F})$. In this paper, we limit the strain energy function to isotropic behavior throughout the deformation history. Isotropic hyperelastic materials can be expressed as a function of strain invariants of the right symmetric Cauchy–Green tensor, $\mathbf{C} = {}^t\mathbf{F}\cdot\mathbf{F}$. Therefore, the strain energy potential can be formulated as

$$\Psi = \Psi(\mathbf{C}) = \Psi(I_1, I_2, I_3), \tag{1}$$

in which

$$I_1 = \mathrm{tr}(\mathbf{C}), \tag{2}$$

$$I_2 = \frac{1}{2}\left[(\mathrm{tr}(\mathbf{C}))^2 - \mathrm{tr}(\mathbf{C}^2)\right], \tag{3}$$

$$I_3 = \det(\mathbf{C}) = [\det(\mathbf{F})]^2 = J^2. \tag{4}$$

One can obtain the derivatives of invariants with respect to $\mathbf{C}$ as follows:

$$\frac{\partial I_1}{\partial \mathbf{C}} = \frac{\partial[\mathrm{tr}(\mathbf{C})]}{\partial \mathbf{C}} = \mathbf{I}, \tag{5}$$

$$\frac{\partial I_2}{\partial \mathbf{C}} = \frac{1}{2}\left[2\mathrm{tr}(\mathbf{C})\mathbf{I} - \frac{\partial[\mathrm{tr}(\mathbf{C}^2)]}{\partial \mathbf{C}}\right] = I_1\mathbf{I} - \mathbf{C}, \tag{6}$$

$$\frac{\partial I_3}{\partial \mathbf{C}} = \frac{\partial J^2}{\partial \mathbf{C}} = I_3\mathbf{C}^{-1}. \tag{7}$$

Thus, the second Piola–Kirchhoff stress tensor can be expressed as

$$\begin{aligned}\mathbf{S} &= 2\frac{\partial \Psi}{\partial \mathbf{C}} = 2\left(\frac{\partial \Psi}{\partial I_1}\frac{\partial I_1}{\partial \mathbf{C}} + \frac{\partial \Psi}{\partial I_2}\frac{\partial I_2}{\partial \mathbf{C}} + \frac{\partial \Psi}{\partial I_3}\frac{\partial I_3}{\partial \mathbf{C}}\right)\\ &= 2\left[\left(\frac{\partial \Psi}{\partial I_1} + I_1\frac{\partial \Psi}{\partial I_2}\right)\mathbf{I} - \frac{\partial \Psi}{\partial I_2}\mathbf{C} + I_3\frac{\partial \Psi}{\partial I_3}\mathbf{C}^{-1}\right].\end{aligned} \tag{8}$$

Several forms of the strain energy function have been proposed in the literature to represent the isotropic hyperelastic material behavior. The most popular one used in the literature is the Ogden model for modeling rubberlike materials. The compressible Ogden constitutive law Ogden, 1984 is described in function of the eigenvalues λ_i $(i = 1, 2, 3)$ of the right Cauchy–Green tensor $\mathbf{C}$ as follows:

$$\Psi = \sum_{i=1}^{N}\frac{\mu_i}{\alpha_i}\left(\lambda_1^{\alpha_i/2} + \lambda_2^{\alpha_i/2} + \lambda_3^{\alpha_i/2} - 3\right) + \sum_{i=1}^{N}\frac{\mu_i}{\alpha_i\beta_i}\left(J^{-\alpha_i\beta_i} - 1\right), \tag{9}$$

where N is a material constant, and μ_i, α_i and β_i are temperature-dependent material parameters.

The Mooney–Rivlin model and neo-Hookean form can be obtained as a particular case of the Ogden model (see Holzapfel, 2000). The compressible form of the Mooney–Rivlin reads

$$\Psi = c(J-1)^2 - d\log(J) + c_1(I_1 - 3) + c_2(I_2 - 3), \tag{10}$$

where c and d are temperature-dependent material parameters, and $c_1 = \mu_1/2$ and $c_2 = -\mu_2/2$ are material constants. By prescribing that the reference configuration is stress-free, we can obtain $d = 2(c_1 + 2c_2)$. One can deduce the second Piola–Kirchhoff stress tensor from Eqs. (8) and (10):

$$\mathbf{S} = 2(c_1 + c_2I_1)\mathbf{I} - 2c_2\mathbf{C} + [2cJ(J-1) - d]\mathbf{C}^{-1}. \tag{11}$$

The neo-Hookean model can be deduced from the strain energy of Mooney–Rivlin (10) by taking $c_2 = 0$. Another version of the neo-Hookean model, which is an extension of linear isotropic constitutive law to large deformation, can be written as

$$\Psi = \frac{1}{2}\lambda_0(\ln J)^2 - \mu_0\ln J + \frac{1}{2}\mu_0(I_1 - 3), \tag{12}$$

where λ_0 and μ_0 are Lamé's material constants. The second Piola–Kirchhoff stress tensor then reads

$$\mathbf{S} = (\lambda_0\ln J - \mu_0)\mathbf{C}^{-1} + \mu_0\mathbf{I}. \tag{13}$$

In this paper, the neo-Hookean law (13) will be chosen in the numerical calculations as often performed in the recent literature (Cao and Hutchinson, 2012a,b; Sun et al., 2012; Zang et al., 2012), while other hyperelastic laws such as Mooney–Rivlin (11) and Gent (1996) can also be straightforward implemented in our modeling and later presented resolution strategy following the same manner. In addition, 8-node linear block elements with reduced integration are applied to discretize the substrate, with totally 24 degrees of freedom per element.

2.2. Nonlinear shell formulation for the film

Challenges in the numerical modeling of such film/substrate systems come from the large aspect ratio ($L_x/h_f \geqslant \mathcal{O}(10^2)$, $L_y/h_f \geqslant \mathcal{O}(10^2)$) and the thickness difference ($h_s/h_f \geqslant \mathcal{O}(10)$), which requires very fine mesh if employing 3D block elements both for the film and for the substrate. Since finite rotations of middle surface and small strains are considered in the thin film, nonlinear shell formulations are quite suitable and efficient for modeling. Hereby, a three-dimensional shell formulation proposed by Büchter et al. (1994) is applied. It is based on a 7-parameter theory including a linear varying thickness stretch as extra variable, which allows applying a complete 3D constitutive law without condensation. It is distinguished from classical shell models that are usually based on degenerated constitutive relations (*e.g.* Kirchhoff–Love, Reissner–Mindlin theories). It is also incorporated via the enhanced assumed strain (EAS) concept proposed by Simo and Rifai (1990) to improve the element performance and to avoid locking phenomena such as Poisson thickness locking, shear locking or volume locking. This hybrid shell formulation can describe large deformation problems such as hyperelasticity and has been successively applied to nonlinear elastic thin-walled structures such as cantilever beam, square plate, cylindrical roof and circular deep arch (Zahrouni et al., 1999; Boutyour et al., 2004).

Geometry and kinematics of shell element are illustrated in Fig. 2, where the position vectors are functions of curvilinear coordinates $(\theta^1, \theta^2, \theta^3)$. The geometry description relies on the middle surface coordinates θ^1 and θ^2 of the shell, while θ^3 represents the coordinate in the thickness direction. The current configuration is defined by the middle surface displacement and the relative displacement between the middle and the upper surfaces. The large

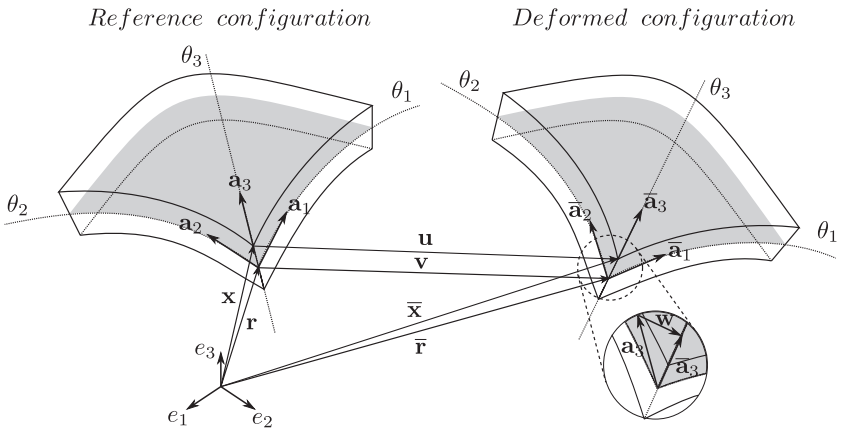

Fig. 2. Geometry and kinematics of shell.

rotations are taken into account without any rotation matrix since the current direction vector is obtained by adding a vector to one of the initial configurations.

In the initial undeformed configuration, the position vector $\mathbf{x}$ representing any point in the shell can be defined as

$$\mathbf{x}(\theta^\alpha, \theta^3) = \mathbf{r}(\theta^\alpha) + \theta^3 \mathbf{a}_3(\theta^\alpha), \tag{14}$$

where $\mathbf{r}(\theta^\alpha)$ $(\alpha = 1, 2)$ denotes the projection of $\mathbf{x}$ in the middle surface and θ^3 describes its perpendicular direction with $\theta^3 \in [-h_f/2, h_f/2]$ in which h_f is the reference thickness of shell. The normal vector of middle surface is represented by $\mathbf{a}_3 = \mathbf{a}_1 \times \mathbf{a}_2$.

Similarly, in the current deformed configuration, we define the position of point $\mathbf{x}$ by the vector $\bar{\mathbf{x}}$:

$$\bar{\mathbf{x}}(\theta^\alpha, \theta^3) = \bar{\mathbf{r}}(\theta^\alpha) + \theta^3 \bar{\mathbf{a}}_3(\theta^\alpha), \tag{15}$$

where

$$\begin{cases} \bar{\mathbf{r}} = \mathbf{r} + \mathbf{v}, \\ \bar{\mathbf{a}}_3 = \mathbf{a}_3 + \mathbf{w}. \end{cases} \tag{16}$$

Therefore, the displacement vector associated with an arbitrary material point in the shell, linearly varies along the thickness direction reads

$$\mathbf{u}(\theta^\alpha, \theta^3) = \bar{\mathbf{x}} - \mathbf{x} = \mathbf{v}(\theta^\alpha) + \theta^3 \mathbf{w}(\theta^\alpha). \tag{17}$$

Totally, six degrees of freedom can be distinguished in Eq. (17) to describe the shell kinematics: three vector components related to the translation of the middle surface (v_1, v_2, v_3) and other three components updating the direction vector (w_1, w_2, w_3).

The Green–Lagrange strain tensor is used to describe geometrical nonlinearity, which can be expressed in the covariant base:

$$\gamma = \frac{1}{2}(\bar{g}_{ij} - g_{ij})\mathbf{g}^i \otimes \mathbf{g}^j \quad with \quad i,j = 1,2,3, \tag{18}$$

where $\mathbf{g}^i$ are the contravariant base vectors, while $g_{ij} = \mathbf{g}^i \cdot \mathbf{g}^j$ and $\bar{g}_{ij} = \bar{\mathbf{g}}^i \cdot \bar{\mathbf{g}}^j$ respectively represent the components of covariant metric tensor in the initial configuration and the deformed one (Büchter et al., 1994).

The hybrid shell formulation is derived from a three-field variational principle based on the Hu-Washizu functional (Büchter et al., 1994; Zahrouni et al., 1999). The stationary condition can be written as

$$\mathbf{\Pi}_f(\mathbf{u}, \tilde{\gamma}, \mathbf{S}) = \int_{\Omega_f} \left\{ {}^t\mathbf{S} : (\gamma_u + \tilde{\gamma}) - \frac{1}{2} {}^t\mathbf{S} : \mathbf{D}^{-1} : \mathbf{S} \right\} d\Omega - \lambda \mathbf{P}_{ext}(\mathbf{u}), \tag{19}$$

where $\mathbf{D}$ is the elastic stiffness tensor. The unknowns are, respectively, the displacement field $\mathbf{u}$, the second Piola–Kirchhoff stress tensor $\mathbf{S}$ and the compatible Green–Lagrange strain γ_u. The enhanced assumed strain $\tilde{\gamma}$, satisfies the condition of orthogonality with respect to the stress field. The work of external load is denoted by $\mathbf{P}_{ext}(\mathbf{u})$, while λ is a scalar load parameter.

Concerning the enhanced assumed strain $\tilde{\gamma}$, classical shell kinematics requires the transversal strain field to be zero ($\gamma_{33} = 0$). In reality, since 3D constitutive relations are concerned, this condition is hardly satisfied due to Poisson effect, especially for bending dominated cases. This phenomenon is commonly referred to as "Poisson thickness locking". To remedy this issue, an enhanced assumed strain $\tilde{\gamma}$ contribution has been introduced in the shell formulation (Büchter et al., 1994), acting across the shell thickness direction and supplementing the compatible strain field γ_u. It describes the linear variation of the thickness stretch or compression, and is expressed with respect to the local curvilinear coordinates θ^3:

$$\tilde{\gamma} = \theta^3 \tilde{\gamma}_{33} \mathbf{g}^3 \otimes \mathbf{g}^3 \quad with \quad \tilde{\gamma}_{33} = \tilde{\gamma}_{33}(\theta^\alpha), \tag{20}$$

and satisfies the condition of orthogonality with respect to the stress field $\mathbf{S}$:

$$\int_{\Omega_f} {}^t\mathbf{S} : \tilde{\gamma} \, d\Omega = 0. \tag{21}$$

In this way, "spurious" transversal strains induced by Poisson effect for bending dominated kinematics are balanced by the assumed strain $\tilde{\gamma}$, which clears the "thickness locking" problem. This approach is applied in this paper, since the associated finite element is very efficient, especially for very thin shells (Zahrouni et al., 1999; Boutyour et al., 2004).

A 8-node quadrilateral element with reduced integration is used for the 7-parameter shell formulation. The enhanced assumed strain $\tilde{\gamma}$ does not require inter element continuity, neither contribute to the total number of nodal degrees of freedom. Therefore, it can be eliminated by condensation at the element level, which preserves the formal structure of a 6-parameter shell theory with totally 48 degrees of freedom per element.

2.3. Coupling between the film and the substrate

As the film is bonded to the substrate, the displacement should be continuous at the interface. However, the shell elements for the film and 3D block elements for the substrate cannot be simply joined directly since they belong to dissimilar elements. Therefore, additional incorporating constraint equations have to be employed. Hereby, Lagrange multipliers are applied to couple the corresponding nodal displacements in compatible meshes between the film and the substrate (see Fig. 3). Note that using 8-node linear block element here is only for coupling convenience,

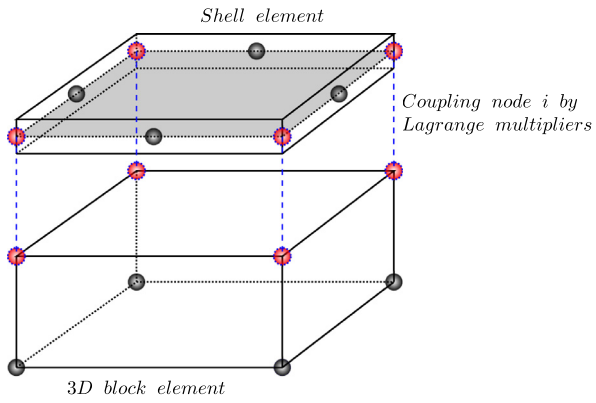

Fig. 3. Sketch of coupling at the interface.

20-node quadratic block element would be another good candidate, while both of them follow the same coupling strategy. Consequently, the stationary function of film/substrate system is given in a Lagrangian form:

$$\mathcal{L}(\mathbf{u}_f, \mathbf{u}_s, \ell) = \mathbf{\Pi}_f + \int_{\Omega_s} \Psi \mathrm{d}\Omega + \sum_{node\ i} \ell_i \left[\mathbf{u}_f^-(i) - \mathbf{u}_s(i) \right], \tag{22}$$

in which

$$\mathbf{u}_f^-(i) = \mathbf{v}(i) - \frac{h_f}{2}\mathbf{w}(i). \tag{23}$$

where the displacements of the film and the substrate are respectively denoted as $\mathbf{u}_f$ and $\mathbf{u}_s$, while the Lagrange multipliers are represented by ℓ. At the interface, the displacement continuity is satisfied at the same nodes and connects the bottom surface of the film ($\mathbf{u}_f^-$) and the top surface of the substrate. From Eq. (22), three equations are obtained according to $\delta\mathbf{u}_f$, $\delta\mathbf{u}_s$ and $\delta\ell$:

$$\begin{cases} \delta\mathbf{\Pi}_f + \sum_{node\ i} \ell_i \delta\mathbf{u}_f^-(i) = 0, \\ \delta \int_{\Omega_s} \Psi \mathrm{d}\Omega - \sum_{node\ i} \ell_i \delta\mathbf{u}_s(i) = 0, \\ \sum_{node\ i} \delta\ell_i \mathbf{u}_f^-(i) - \sum_{node\ i} \delta\ell_i \mathbf{u}_s(i) = 0. \end{cases} \tag{24}$$

3. Resolution techniques

Asymptotic Numerical Method (ANM) (Damil and Potier-Ferry, 1990; Cochelin et al., 1994, 2007; Cochelin, 1994) is applied to solve the resulting nonlinear equations. The ANM is a path-following technique that is based on a succession of high order power series expansions (perturbation technique) with respect to a well chosen path parameter, which appears as an efficient continuation predictor without any corrector iteration. Besides, one can get approximations of the solution path that are very accurate inside the radius of convergence. In this paper, the main interest of the ANM is its ability to trace the post-buckling evolution and predict secondary bifurcations without any special tool. Precisely, accumulation of small steps in the ANM is often associated with the occurrence of a bifurcation (Xu, 2014; Xu et al., 2014, 2015). Second, to facilitate the computing of the asymptotic coefficients of Taylor series in quadratic forms, Automatic Differentiation (AD) techniques (Griewank, 2000) are employed. The AD techniques can significantly improve the ease of the ANM implementation through an operator overloading (Koutsawa et al., 2008; Charpentier and Potier-Ferry, 2008), which allows one to consider various potential energy functions of hyperelastic laws in a rather simple and efficient manner.

3.1. Path-following technique

The resulting nonlinear problem (24) can be rewritten as

$$\delta\mathcal{L}(\mathbf{u}_f, \mathbf{u}_s, \ell) = \langle \mathbf{R}(\mathbf{U}, \lambda), \delta\mathbf{U} \rangle = 0, \tag{25}$$

where $\mathbf{U} = (\mathbf{u}_f, \mathbf{u}_s, \ell)$ is a mixed vector of unknowns and $\mathbf{R}$ is the residual vector. The external load parameter is denoted as a scalar λ. The principle of the ANM continuation consists in describing the solution path by computing a succession of truncated power series expansions. From a known solution point $(\mathbf{U}_0, \lambda_0)$, the solution $(\mathbf{U}, \lambda)$ is expanded into truncated power series of a perturbation parameter a:

$$\begin{cases} \mathbf{U}(a) = \mathbf{U}_0 + \sum_{p=1}^{n} a^p \mathbf{U}_p, \\ \lambda(a) = \lambda_0 + \sum_{p=1}^{n} a^p \lambda_p, \end{cases} \tag{26}$$

$$a = \langle \mathbf{u} - \mathbf{u}_0, \mathbf{u}_1 \rangle + (\lambda - \lambda_0)\lambda_1, \tag{27}$$

where n is the truncation order of the series. Eq. (27) defines the path parameter a that can be identified to an arc-length parameter. By introducing Eq. (26) into Eqs. (25) and (27), then equating the terms at the same power of a, one can obtain a set of linear problems. More details of these procedures can be found in Cochelin et al. (1994, 2007) and Xu et al. (2014, 2015).

The maximum value of the path parameter a should be automatically defined by analyzing the convergence of the power series at each step. The a_{max} can be based on the difference of displacements at two successive orders that must be smaller than a given precision parameter δ:

$$\text{Validity range}: a_{max} = \left(\delta \frac{\|\mathbf{u}_1\|}{\|\mathbf{u}_n\|} \right)^{1/(n-1)}, \tag{28}$$

where the notation $\|\cdot\|$ stands for the Euclidean norm. Unlike incremental-iterative methods, the arc-length step size a_{max} is adaptive since it is determined *a posteriori* by the algorithm. When there is a bifurcation point on the solution path, the radius of convergence is defined by the distance to the bifurcation. Thus, the step length defined in Eq. (28) becomes smaller and smaller, which looks as if the continuation process "knocks" against the bifurcation (Baguet and Cochelin, 2003). This accumulation of small steps is a very good indicator of the presence of a singularity on the path. All the bifurcations can be easily identified in this way by the user without any special tool.

It is worth mentioning that there are only two parameters controlling the algorithm. The first one is the truncation order n of the series. It was previously discussed that the optimal truncation order should be large enough between 10 and 20, but bigger values (*e.g.* $n = 50$) lead to good results for large scale problems as well (Medale and Cochelin, 2009). Another important parameter is the chosen tolerance δ that affects the residual. For instance, very small values of tolerance (*e.g.* $\delta = 10^{-6}$) ensure quite a high accuracy and a pretty robust path-following process.

3.2. Automatic Differentiation with the ANM

The implementation of the recurrence formulae in the ANM is relatively simple for Föppl–von Kármán nonlinear plate or Navier–Stokes equations (Xu et al., 2015; Xu, 2014), but it can be tedious in a more general constitutive framework. For example, there are several forms of strain energy potentials to describe hyperelastic behavior of rubberlike materials: Ogden, Mooney–Rivlin, neo-Hookean, Gent, Arruda–Boyce, *etc*. Therefore, a generic scheme is required to define Taylor series for all these constitutive

laws. That is why some tools based on Automatic Differentiation (AD) techniques (Griewank, 2000) have been proposed to compute high order derivatives of constitutive laws (Koutsawa et al., 2008; Charpentier and Potier-Ferry, 2008; Lejeune et al., 2012, 2013), which allows one to introduce various potential energy functions of hyperelastic laws in a rather simple and automatic way.

One can write any finite strain hyperelasticity problem in the following generalized form:

$$\begin{cases} \int_\Omega {}^t\mathbf{P} : \delta\mathbf{F}\ \mathrm{d}\Omega = \lambda \mathbf{P}_{ext}(\delta\mathbf{u}), \\ \mathbf{S} = \phi(\boldsymbol{\gamma}), \\ \mathbf{P} = \mathbf{F}\cdot\mathbf{S}, \\ \boldsymbol{\gamma} = \frac{1}{2}({}^t\mathbf{F}\cdot\mathbf{F} - \mathbf{I}), \\ \mathbf{F} = \mathbf{I} + \nabla\mathbf{u}, \end{cases} \tag{29}$$

where $\mathbf{P}$ is the first Piola–Kirchhoff stress tensor. For hyperelastic materials, the stress field $\mathbf{S}$ depends both on elastic material constants and the current strain field, *i.e.* $\mathbf{S} = \phi(\boldsymbol{\gamma})$. This constitutive relation can be any specific form as introduced in Section 2.1, *i.e.* Mooney–Rivlin (11), neo-Hookean (13) and Gent (1996), *etc.*

Different variables of hyperelastic problems can be represented by a mixed vector $\mathbf{V} = (\mathbf{u}, \mathbf{F}, \boldsymbol{\gamma}, \mathbf{S}, \mathbf{P})$ that is then expanded into truncated power series as in Eq. (26). Within the ANM, one has to build the linear equations satisfied by the coefficients of Taylor $\mathbf{V}_p = \left(\mathbf{u}_p, \mathbf{F}_p, \boldsymbol{\gamma}_p, \mathbf{S}_p, \mathbf{P}_p\right)$. Automatic Differentiation (AD) is the most relevant technique in view of applications to generic hyperelastic models. Following the definition of Bischof and Bücker (2000), AD can be viewed as the way to generate a code which computes the derivative of a function itself given by a code. Any function combining elementary operations $(+, -, \times, \div, etc.)$ and elementary functions $(exp, sin, etc.)$ can be differentiated in this way. This study applies the Matlab AD toolbox presented in Koutsawa et al. (2008) to compute the derivatives of the constitutive law $\mathbf{S} = \phi(\boldsymbol{\gamma})$. The AD has been first introduced in the ANM algorithm by Charpentier and Potier-Ferry (2008) to make the algorithm more generic and easier to be implemented. For more details on the ANM, see Cochelin et al. (2007), Xu et al. (2014, 2015) and references cited therein. The theoretical developments based on the generic Faá di Bruno formula for the higher order differentiation of compound functions have been presented in Koutsawa et al. (2008). Because of the relation $\mathbf{S} = \phi(\boldsymbol{\gamma})$, the p-th derivative of the stress $\mathbf{S}_p$ is a function of the derivatives of strain at orders between 0 and p and linearly depends on the last order $\boldsymbol{\gamma}_p$. Hence, it can be written as

$$\mathbf{S}_p\left(\boldsymbol{\gamma}_0, \boldsymbol{\gamma}_1, \ldots, \boldsymbol{\gamma}_p\right) = \mathbb{C}_t : \boldsymbol{\gamma}_p + \mathbf{S}_p^{res}, \tag{30}$$

where

$$\mathbf{S}_p^{res} = \mathbf{S}_p\left(\boldsymbol{\gamma}_0, \boldsymbol{\gamma}_1, \ldots, \boldsymbol{\gamma}_{p-1}, 0\right). \tag{31}$$

The fourth order tensor $\mathbb{C}_t$ is the classical tangent modulus tensor and depends on both the elastic material constants and the current stress field. Material nonlinearity induces a residual term $\mathbf{S}_p^{res}$ that depends on the solutions computed at the previous orders and that can be computed as the p-th derivative of $\mathbf{S}_p$ for $\boldsymbol{\gamma}_p = 0$ (see Charpentier and Potier-Ferry, 2008). This generic ANM algorithm has been implemented in a Matlab AD toolbox named Diamant that is applied to compute the ANM right hand sides $\mathbf{S}_p^{res}$. The tangent modulus tensor $\mathbb{C}_t$ can be built from the relation (30) at order $p = 1$, by choosing any tensor $\boldsymbol{\gamma}_1$ in the canonical basis. The derivatives in tangent modulus tensor $\mathbb{C}_t$ can be computed through operator overloading techniques by directly applying AD toolboxes such as TOMLAB/MAD (Forth and Edvall, 2007) in Matlab or the package ADOL-C (Walther and Griewank, 2010) in C/C++. In this paper, we employ TOMLAB/MAD in Matlab environment for convenience.

The four other equations in (29) are generic equations of continuum mechanics and they are linear or quadratic with respect to the unknown $\mathbf{V}$. Thus, the corresponding recurrence formulae are straightforward and can be found in several papers, for example in Nezamabadi et al. (2011). The displacement–strain relation and the connection between the two stress tensors $\mathbf{P}$ and $\mathbf{S}$ can be written as

$$\begin{cases} \boldsymbol{\gamma}_p = \frac{1}{2}\left({}^t\mathbf{F}_0\cdot\nabla\mathbf{u}_p + {}^t\nabla\mathbf{u}_p\cdot\mathbf{F}_0\right) + \boldsymbol{\gamma}_p^{nl}, \\ \boldsymbol{\gamma}_p^{nl} = \frac{1}{2}\left(\sum_{r=1}^{p-1} {}^t\mathbf{F}_{p-r}\cdot\mathbf{F}_r\right), \\ \mathbf{P}_p = \mathbf{F}_0\cdot\mathbf{S}_p + \nabla\mathbf{u}_p\cdot\mathbf{S}_0 + \mathbf{P}_p^{res}, \\ \mathbf{P}_p^{res} = \sum_{r=1}^{p-1}\mathbf{F}_{p-r}\cdot\mathbf{S}_r. \end{cases} \tag{32}$$

By considering Eq. (30), this leads to a constitutive relation connecting Taylor coefficients of the displacement gradient $\nabla\mathbf{u}$ and the first Piola–Kirchhoff stress tensor $\mathbf{P}$:

$$\begin{cases} \mathbf{P}_p = \mathbb{H} : \nabla\mathbf{u}_p + \mathbf{P}_p^{nl}, \\ \mathbf{P}_p^{nl} = \mathbf{F}_0\cdot\mathbb{C}_t : \boldsymbol{\gamma}_p^{nl} + \mathbf{P}_p^{res}, \\ \mathbb{H} = \psi(\mathbf{F}_0, \mathbf{S}_0, \mathbb{C}_t), \end{cases} \tag{33}$$

where $\mathbb{H}$ is a fourth order tensor and can be expressed as a function of deformation gradient tensor $\mathbf{F}_0$, the second Piola–Kirchhoff stress tensor $\mathbf{S}_0$ and the tangent modulus tensor $\mathbb{C}_t$, depending only on the initial state (Nezamabadi et al., 2011). Thus, this tangent stiffness matrix is updated at each ANM step, see Eq. (35) depending only on the initial state at the beginning of the ANM step. The details can be found in Appendix A.

These formulae can now be introduced in the balance of momentum and this leads to a classical linear equation that can be easily discretized by finite element method:

$$\mathbf{L}_t^0(\mathbf{u}_p, \delta\mathbf{u}) = \lambda_p \mathbf{P}_{ext}(\delta\mathbf{u}) + \mathcal{F}_p^{nl}(\delta\mathbf{u}), \tag{34}$$

where $\mathbf{L}_t^0$ is the tangent stiffness matrix depending only on the initial solution:

$$\mathbf{L}_t^0(\mathbf{u}_p, \delta\mathbf{u}) = \int_\Omega {}^t\nabla\mathbf{u}_p : \mathbb{H} : \nabla\delta\mathbf{u}\ \mathrm{d}\Omega. \tag{35}$$

The nonlinear term $\mathcal{F}_p^{nl}$ is a residual vector that is null at order 1, while at order p it is expressed as

$$\mathcal{F}_p^{nl}(\delta\mathbf{u}) = -\int_\Omega {}^t\mathbf{P}_p^{nl} : \nabla\delta\mathbf{u}\mathrm{d}\Omega \quad with \quad 1 < p \leqslant n. \tag{36}$$

4. Numerical results and discussion

Spatial wrinkling patterns of thin films on hyperelastic substrates will be investigated under different loading and boundary conditions. The computation technique has been chosen to avoid most of the restrictive assumptions that are generally done in the literature (Chen and Hutchinson, 2004; Huang et al., 2005; Audoly and Boudaoud, 2008a): here the considered domain is three-dimensional, the finite element discretization allows accounting for any initial configuration and any boundary condition, the finite strain framework represents exactly the geometry and the path-following technique provides the response of the system beyond the primary bifurcation. Similar to some recent studies (Brau et al., 2011; Cao and Hutchinson, 2012a; Yin et al., 2012), the ratio of Young's modulus, E_f/E_s, is generally chosen in the range $\mathcal{O}(10)$. In the present paper, we limit ourselves to neo-Hookean substrates, which is the finite strain hyperelastic constitutive law generally considered in the recent literature, even though the

implementation of various constitutive laws is easy with Automatic Differentiation procedure described in Section 3.2. Nevertheless, many works in the literature assume a linear elastic substrate and the range of validity of this hypothesis has been rarely discussed. That is why we will compare these two assumptions and the stiffness ratio, E_f/E_s, will be a critical parameter in this discussion.

The material and geometric properties of the film/substrate system are similar to those in Brau et al. (2011), Cao and Hutchinson (2012a) and Yin et al. (2012), which is shown in Table 1. The different dimensional parameters and loading conditions for each case are presented in Table 2 and Fig. 4, respectively. In this paper, the force loading is applied to the film. On the bottom surface of the substrate, the deflection u_z and the tangential traction are taken to be zero. Poisson's ratio is a dimensionless measure of the degree of compressibility. Compliant materials in the substrate, such as elastomers, are nearly incompressible with $\nu_s = 0.48$. As for neo-Hookean hyperelastic law, Lamé's first parameter is expressed as $\lambda_0 = E_s\nu_s/[(1+\nu_s)(1-2\nu_s)]$, while the shear modulus is denoted as $\mu_0 = E_s/[2(1+\nu_s)]$.

In order to trigger a transition from the fundamental branch to the bifurcated one, small perturbation forces, $f_z = 10^{-8}$, are imposed on each node of the shell elements in the film at every loading step. These perturbation forces are involved in the external force vector $\mathbf{P}_{ext}$ in the equilibrium Eq. (34), by multiplying the loading parameter λ_p at each ANM step. The introduction of such small perturbation forces is quite a common technique in the solution of bifurcation problems by continuation techniques (Doedel, 1981; Allgower and Georg, 1990), even when using commercial finite element codes. This artifice could be avoided by applying a specific procedure to compute the bifurcation branch as in Boutyour et al. (2004) and Vannucci et al. (1998). In this paper, the perturbation forces f_z allow one to compute the whole bifurcated branch with a single continuation algorithm. The number of elements required for a convergent solution was carefully examined. The way that we took is similar as in Xu et al. (2015), by testing a number of different meshes in three directions. In this paper, we detect bifurcation points by the criterion of small step accumulation. Indeed, when the starting point of the step is close to the bifurcation, the radius of convergence of Taylor series coincides with the distance to the singular point, which explains that the continuation process 'knocks' against the bifurcation (Baguet and Cochelin, 2003). Of course the same step accumulation is observed for a slightly perturbed bifurcation that we shall call quasi-bifurcation. More advanced techniques are available for bifurcation detection such as bifurcation indicator (Xu et al., 2014, 2015) and power series analysis in Cochelin and Medale (2013), but the simple detection by sight will prove to be sufficient in our analyses. In what follows, we will explore the formation and evolution of 3D instability modes including folds, occurring due to the nonlinearity of substrate in the case of a not too large wave number. Provided that sufficient computer resources are available, the presented

Table 1
Common characteristics of material and geometric properties.

E_f (MPa)	E_s (MPa)	ν_f	ν_s	h_f (mm)	h_s (mm)
1.3×10^2	1.8	0.4	0.48	10^{-2}	0.1

Table 2
Different film/substrate systems.

	L_x (mm)	L_y (mm)	Loading
Film/Sub I	1.5	1.5	Uniaxial
Film/Sub II	1	1	Equi-biaxial

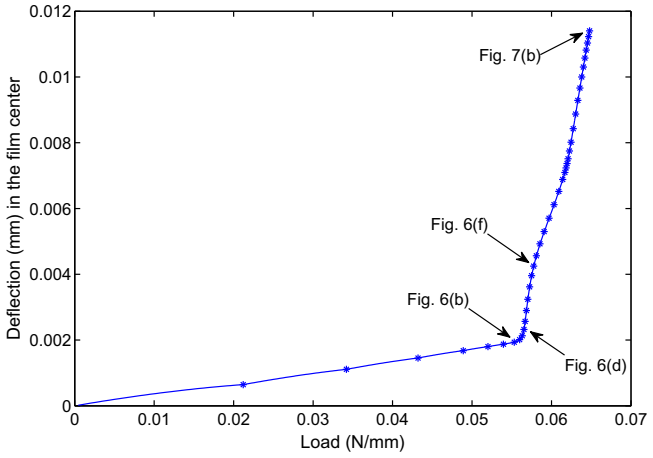

Fig. 5. Bifurcation curve of Film/Sub I with simply supported boundary conditions under uniaxial compression. Representative wrinkling shapes in Figs. 6 and 7 on the post-buckling evolution path are marked. ANM parameters: $n = 10, \delta = 10^{-5}$, 40 steps. Each point corresponds to one ANM step.

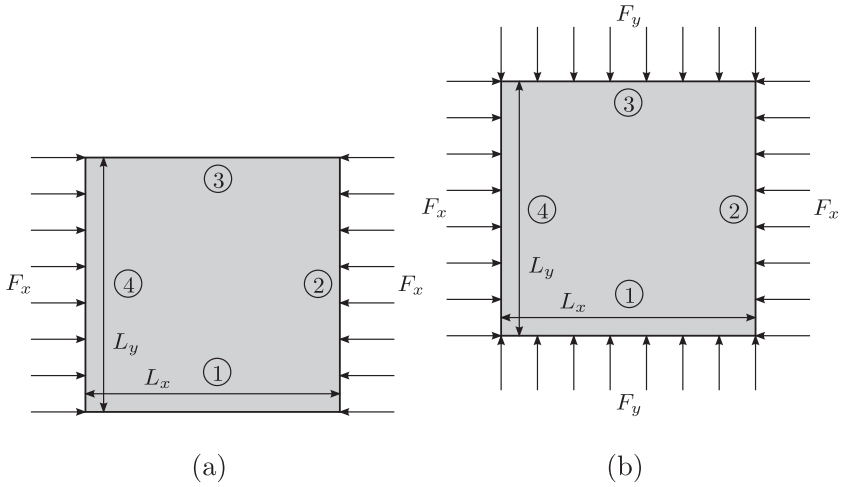

Fig. 4. Loading conditions: (a) Film/Sub I under uniaxial compression, (b) Film/Sub II under equi-biaxial compression.

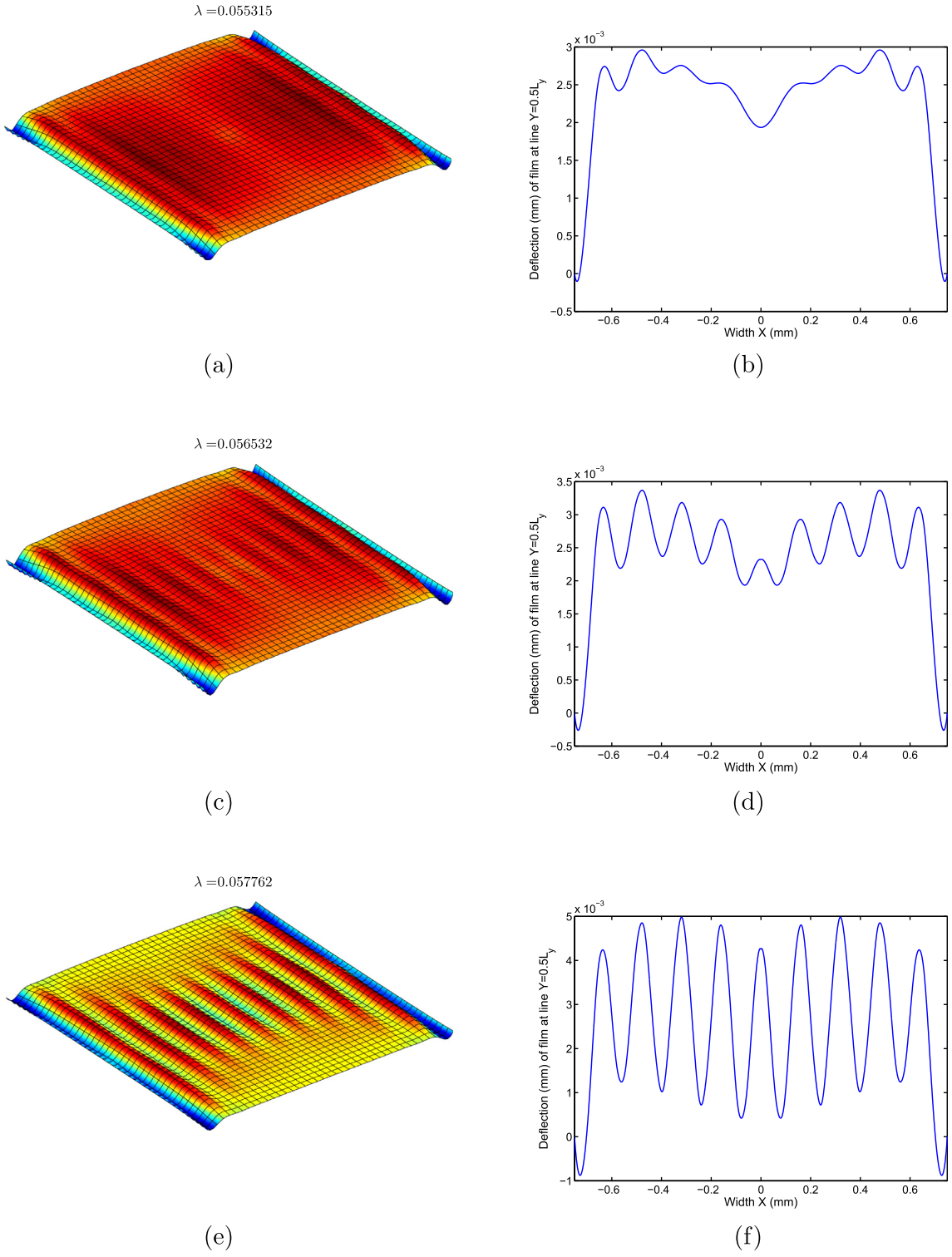

Fig. 6. Film/Sub I with simply supported boundary conditions under uniaxial compression. The left column shows a sequence of wrinkling patterns on the evolution path. The right column presents the associated instability shapes at the line $Y = 0.5L_y$.

model does not show any strict limitation to simulate a large sample with huge wave number. However, due to the limitation of computer capacity, it took about two or three days even for simulating the small samples that we considered in this study. In this respect, an idea for simulating larger samples is to consider reduced-order models, for example via the technique of slowly variable Fourier coefficients (Damil and Potier-Ferry, 2010).

4.1. Uniaxial compression

First, we investigate the pattern formation and evolution via Film/Sub I. The film is uniaxially compressed along the x direction as shown in Fig. 4(a). The displacements v_2, v_3, w_2 and w_3 are taken to be zero on loading sides ② and ④ (see Fig. 4(a)) that are parallel to O_y. This means that these sides are simply supported because

the rotation w_1 around O_y is not locked. The other two sides ① and ③ are set to be free. To avoid rigid body motions, the displacement v_1 in the film center is locked as well. The film is meshed with 40×40 shell elements to ensure at least four elements within a single wave. The substrate is compatibly discretized by 6400 block elements with four layers. Totally, the film/substrate system contains 60024 degrees of freedom (DOF) including the Lagrange multipliers.

The critical load of sinusoidal wrinkles based on classical linearized stability analysis was presented in Chen and Hutchinson (2004) and Huang et al. (2005), with Föppl–von Kármán nonlinear elastic plate assumption for the film and linear elasticity for the material. For a thick substrate, the critical load is expressed as $F_c = 1/4 h_f \bar{E}_f (3\bar{E}_s/\bar{E}_f)^{2/3}$, where $\bar{E}_f = E_f/\left(1-\nu_f^2\right)$ and $\bar{E}_s = E_s/(1-\nu_s^2)$. By introducing the material and geometric parameters in Table 1, one can obtain the analytical solution for periodic boundary conditions $F_c = 0.049$ N/mm, which is comparable to our 3D finite element results with hyperelastic materials and real boundary conditions (about 0.055 N/mm in Fig. 5).

The established 3D model based on the ANM offers a very fast computing speed to reach the critical point with few steps (see Fig. 5). The deflection v_3 in the film center is depicted in bifurcation curves. The accumulation of small steps indicates the presence of quasi-bifurcation points for about $v_3 = 0.007$ mm and $v_3 = 0.011$ mm. The sequence of wrinkling patterns on the load–displacement curve are illustrated in Fig. 6. A surface localized valley, but not a fold that typically happens much later than the first bifurcation, occurs in the center of the film as shown in Fig. 6(b). This kind of mode is probably due to the substrate nonlinearity (Cai and Fu, 1999; Hutchinson, 2013) and has not been observed with a linear elastic substrate (Xu et al., 2014). The localization of boundary effects can also be observed near the sides ② and ④, which corresponds to the regions where compressive stresses are larger. When the load increases, a small ridge shape occurs and grows in the valley (see Fig. 6(d) and (f)). In the end, boundary effects are not so obvious and a weak decrease of the amplitude appears in the center.

Following the same strategy, we investigate the surface morphological instability via Film/Sub I in the case of clamped boundary conditions. More specifically, the displacements w_1 is also taken to be zero on loading sides ② and ④ (see Fig. 4(a)) that are parallel to O_y. This means that these sides are clamped because the rotation w_1 around O_y is locked. The other boundary conditions and loadings are the same as before. The same mesh as in simply supported case is carried out.

The bifurcation diagram and the corresponding wrinkling patterns are respectively demonstrated in Figs. 8 and 9. The instability mode evolution in the bulk is almost the same as with the simply supported case, while the difference appears near the boundary. In addition, the pattern demonstrates undulation localization around the second and the third oscillations when the load reaches the final step (see Fig. 10).

At the end of the response curves in Figs. 5 and 8, a small step accumulation and a maximal load point were found. The pattern form has no change at this level without appearing localized folds. In the literature, some extremely localized instability modes such as folding and ridging are only observed in 2D plane strain simulation of planar film/substrate system, but not in 3D system. The continuation process was difficult to manage after this subcritical bifurcation. Hence, one can assert that an unstable bifurcation point occurs before the strain corresponding to folds in 2D cases. The continuation algorithm has not allowed searching such folds by following the solution branch. Complementary studies should be carried out, perhaps with alternative solution techniques. Likely these very unstable bifurcations do not result from an artefact of the shell/3D model because we recently obtain similar results from a 3D/3D model.

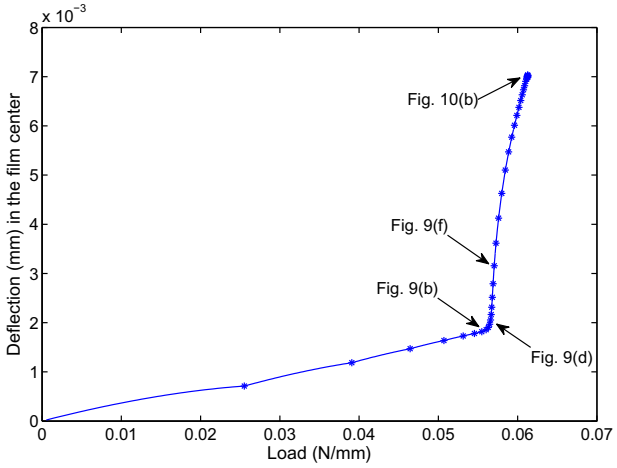

Fig. 8. Bifurcation curve of Film/Sub I with clamped boundary conditions under uniaxial compression. Representative wrinkling shapes in Figs. 9 and 10 on the post-buckling evolution path are marked. ANM parameters: $n = 10, \delta = 10^{-5}$, 40 steps. Each point corresponds to one ANM step.

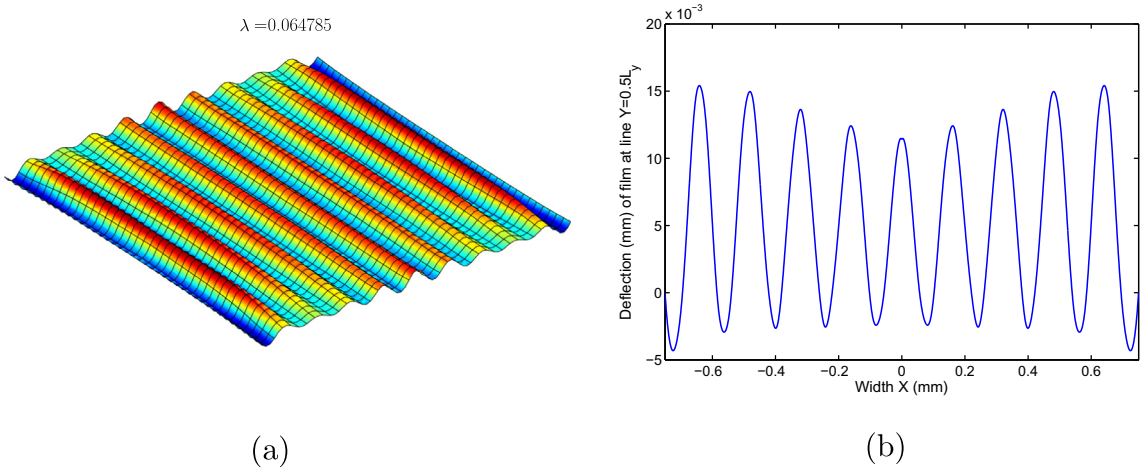

Fig. 7. Film/Sub I with simply supported boundary conditions under uniaxial compression: (a) sinusoidal pattern in the final step, (b) the final shape with modulation.

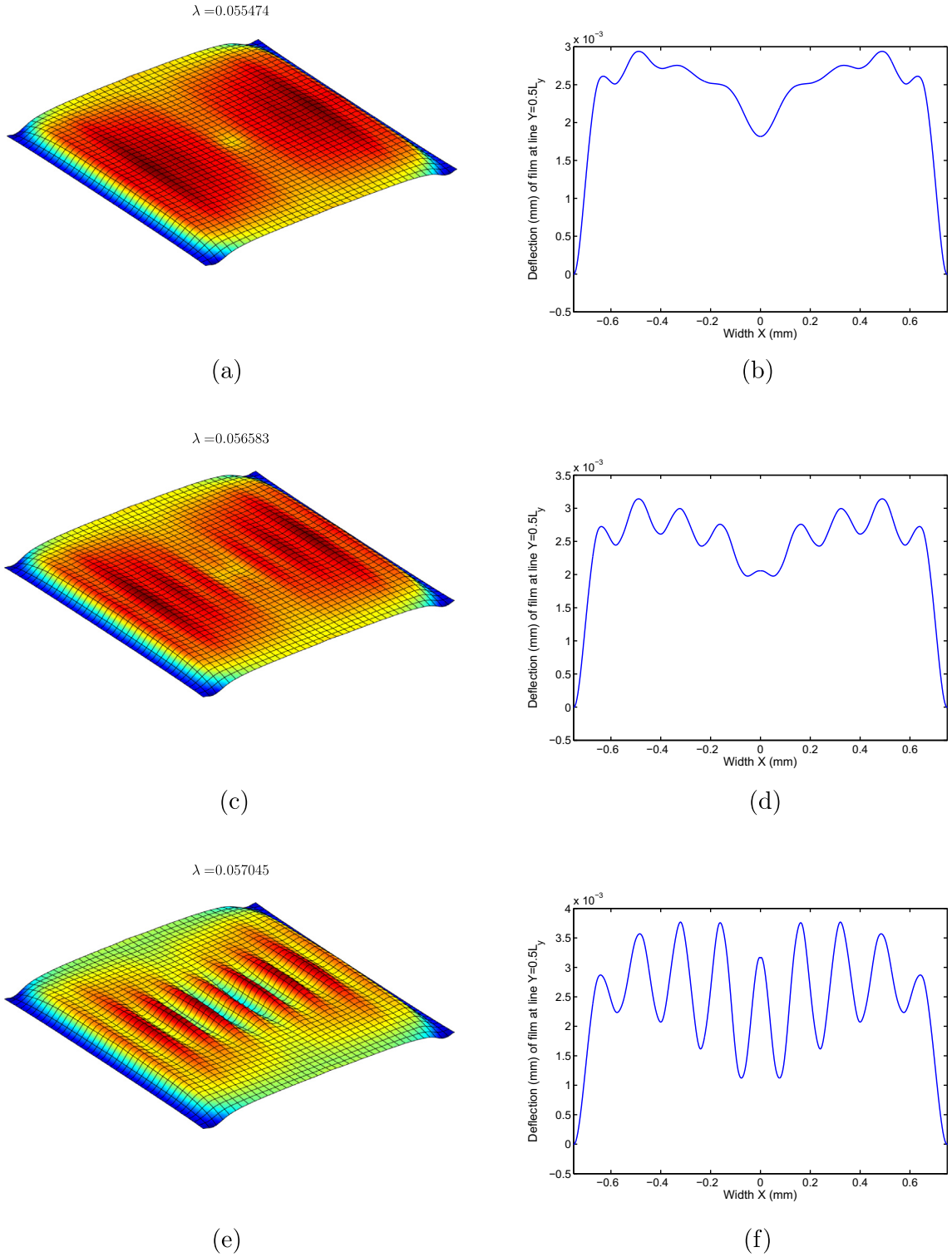

Fig. 9. Film/Sub I with clamped boundary conditions under uniaxial compression. The left column shows a sequence of wrinkling patterns on the evolution path. The right column presents the associated instability shapes at the line $Y = 0.5L_y$.

4.2. Equi-biaxial compression

Three-dimensional instability modes are then explored via Film/Sub II under equi-biaxial compression both in x and y direction (see Fig. 4(b)). The deflections v_3 on four edges ①, ②, ③ and ④, are locked to be zero, which means the film is simply supported on the whole boundary. The displacements v_1 and v_2 in the film center are also set to be zero so as to avoid rigid body motions. The same mesh as in the uniaxial compression case with totally 60024 DOF is maintained.

The ANM takes very big step lengths to reach the critical load, then the step length automatically shortens around the bifurcation (see Fig. 11). Fig. 12 presents a sequence of representative wrinkling patterns on the post-buckling response curves in Fig. 11. In

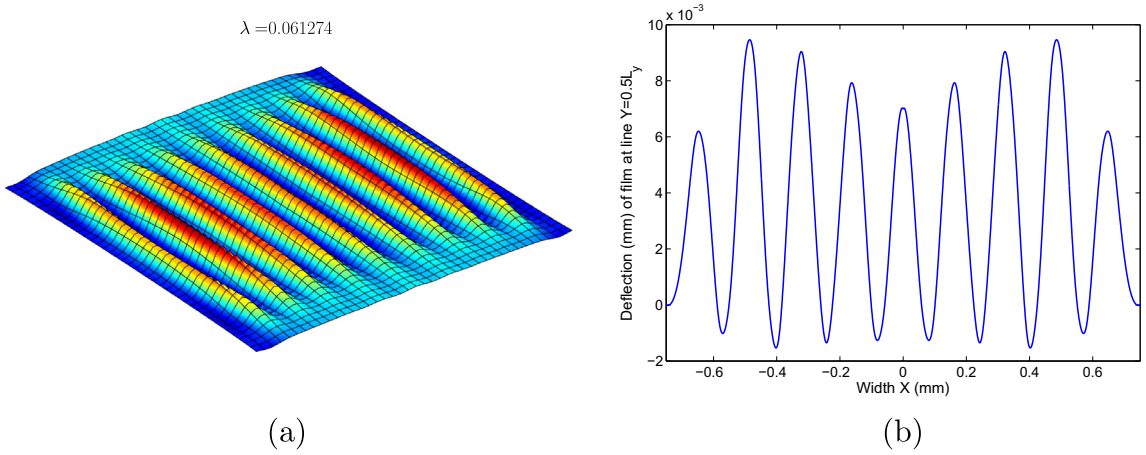

Fig. 10. Film/Sub I with clamped boundary conditions under uniaxial compression: (a) sinusoidal pattern in the final step, (b) the final shape with localization.

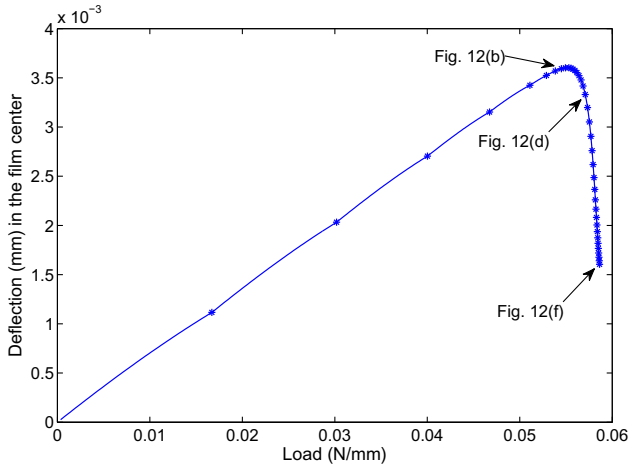

Fig. 11. Bifurcation curve of Film/Sub II under equi-biaxial compression. Representative wrinkling shapes in Fig. 12 on the post-buckling evolution path are marked. ANM parameters: $n = 10, \delta = 10^{-6}$, 37 steps. Each point corresponds to one ANM step.

the initial stage, the pattern is not uniform and one observes a fold-like wrinkle shape in the middle. Boundary and corner effects appear as well due to stress concentration in these areas. Then this mode grows with respect to the external incremental load and the folding shape tends to be more apparent (see Fig. 12(d)). The wrinkling pattern in the final step is depicted in Fig. 12(e), which demonstrates a more uniform and stable checkerboard mode compared with the one obtained in the framework of a linear elastic substrate (Xu et al., 2014).

4.3. Comparisons between neo-Hookean and linear elasticity

We compare the bifurcation diagrams (see Fig. 13) between the presented neo-Hookean hyperelastic model and the linear elastic model previously established in Xu et al. (2014). Both of them share the same critical load and the post-buckling evolution trends, while the deflection in the linear elastic model is slightly bigger than that in the neo-Hookean hyperelastic model. This is reasonable since the stiffness of the neo-Hookean substrate increases with respect to the incremental compression. The comparison of pattern shapes is illustrated in Fig. 14. It can be seen that the hyperelastic model shows a more uniformly distributed checkerboard mode with little boundary effects compared with the linear elastic model where the pattern tends to be 1D mode near the boundary. Besides, the neo-Hookean hyperelastic model reveals a non-symmetric square checkerboard pattern, while the linear elastic model maintains perfect symmetry throughout the path. It appears that finite strain hyperelastic model such as neo-Hookean can well describe the checkerboard shape when the slopes of the film increase (see Fig. 14), and the nonlinearity of the substrate would lead to the appearance of weak localization (see Fig. 12). In the present 3D cases, some extremely localized instability modes explored recently, such as folding (Sun et al., 2012) or ridging (Zang et al., 2012), obtained from 2D plane strain simulation, have not been found here.

Another comparisons between the two models according to the stiffness ratio of Young's modulus, E_f/E_s, are performed in Figs. 15 and 16 to investigate the differences between the hyperelastic model and linear elastic one. One can find that when the film becomes stiffer, the bifurcation curves of two models tend to be qualitatively similar, at least following the same trends, since the compressive strain $\overline{\gamma}_{xx}$ is quite small (less than 1.4% in Fig. 15) and thus the linear elastic framework is relevant. It can be expected that in the case of a larger stiffness ratio $E_f/E_s \gg 10^3$, *e.g.* in the range $\mathcal{O}(10^5)$ as chosen in Xu et al. (2014), the two models should be quantitatively equivalent since the deformation must be infinitesimal. On the contrary, when the film becomes softer, *e.g.* $E_f/E_s = 30$ in the range $\mathcal{O}(10)$, differences between the bifurcation curves tend to be significant. One can see that the compressive strain $\overline{\gamma}_{xx}$ reaches rather large values (up to 13% in Fig. 16) and linear elastic model is no more appropriate. In this case, finite strain models such as neo-Hookean hyperelasticity should be considered. Nevertheless, if the film is too soft for example with $E_f/E_s = 7.2$ in the range $\mathcal{O}(1)$, the film/substrate system undergoes a global buckling deformation without local wrinkling. The post-buckling curves of both models become very unstable after a linear response as shown in Fig. 17. The maximum load point is lower in the case of a neo-Hookean substrate. It is worth mentioning that two bifurcations are clearly observed on each curve in Fig. 15. The first one corresponds to a boundary effect mode, with global Poisson effect deformation and a small surface valley in the center, like Fig. 12(b). Then the amplitude grows, so that the deflection turns out to be minus value around the second bifurcation. The second bifurcation shows a square checkerboard shape, still with a valley in the center, like Fig. 12(f). After the second bifurcation, the valley starts to gradually change to a peak and finally achieves.

For clarity, the comparisons between a neo-Hookean and a linear elastic substrate have been summarized in Table 3. As for a

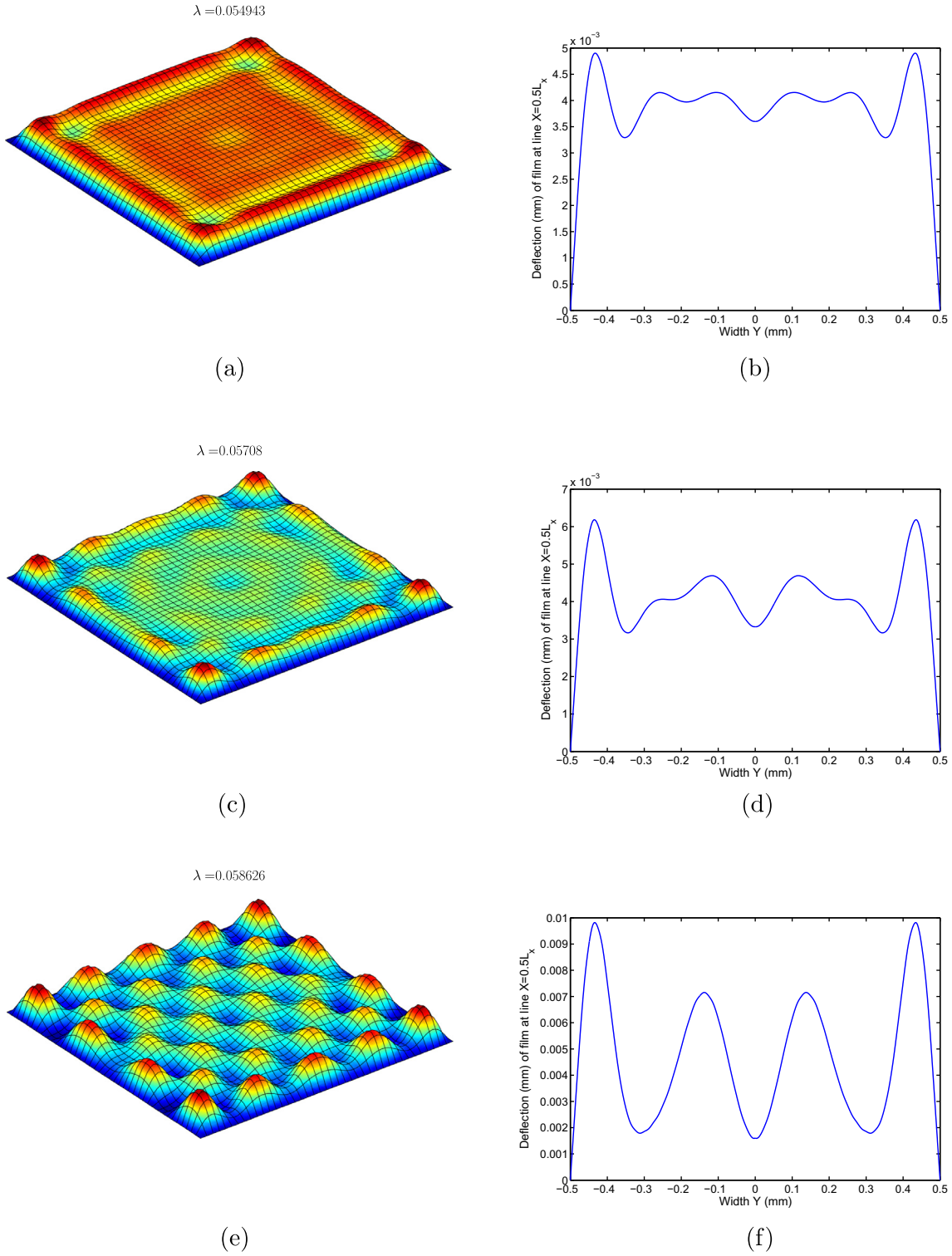

Fig. 12. Film/Sub II with $E_f/E_s = 72$ ($E_f = 130$ MPa, $E_s = 1.8$ MPa) under equi-biaxial compression. The left column shows a sequence of wrinkling patterns on the evolution path. The right column presents the associated instability shapes at the line $X = 0.5L_x$.

large stiffness ratio, the first bifurcation load is small (about 1.2%). The critical load and the post-bifurcation behavior are more or less similar with the two models. Significant differences have been observed in the range $E_f/E_s = \mathcal{O}(10)$, where the first bifurcation occurs for larger strain values. For instance, when $E_f/E_s = 30$, the first bifurcation occurs later with a neo-Hookean substrate, at a mean strain of 12% instead of 10.2% with a linear elastic law for the substrate. Between 10% and 12%, the model with a linear substrate predicts the appearance of a non-uniformly distributed checkerboard shape with boundary effects, while the response with the neo-Hookean law tends to be periodic in the center. The earlier bifurcation with the linear elastic law indicates a larger stiffness of the neo-Hookean response at these medium strains. As a counterpart, an unstable bifurcation behavior is observed with

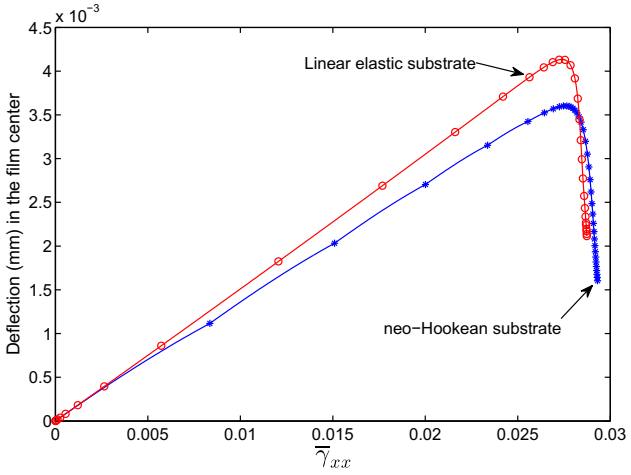

Fig. 13. Comparison of bifurcation curves of Film/Sub II with $E_f/E_s = 72$ ($E_f = 130$ MPa, $E_s = 1.8$ MPa) under equi-biaxial compression. Linear elastic model and neo-Hookean hyperelastic model are depicted together. ANM parameters for linear elastic model: $n = 10, \delta = 10^{-6}$, 63 steps. Each point corresponds to one ANM step.

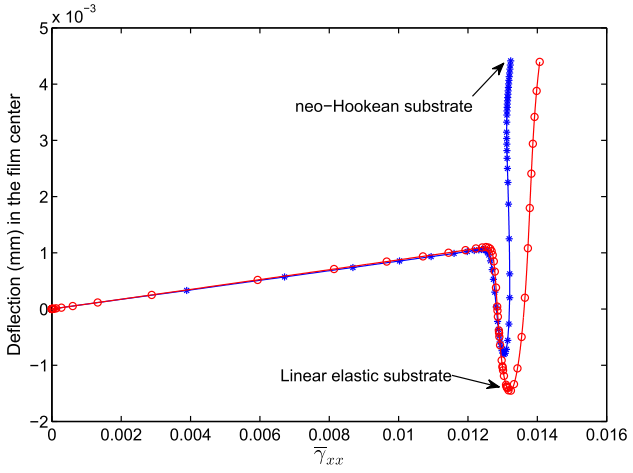

Fig. 15. Comparison of bifurcation curves of stiff films with $E_f/E_s = 722$ ($E_f = 1300$ MPa, $E_s = 1.8$ MPa) under equi-biaxial compression. Linear elastic model and neo-Hookean hyperelastic model are depicted together. ANM parameters for hyperelastic model: $n = 10, \delta = 10^{-6}$, 60 steps. ANM parameters for linear elastic model: $n = 10, \delta = 10^{-6}$, 104 steps. Each point corresponds to one ANM step.

the nonlinear hyperelastic law, while the post-buckling is stable within linear elasticity framework. Is this similar to the behavior of axially compressed cylindrical shells that have both a quite high bifurcation load and a very high imperfection sensitivity? For the smallest stiffness ratio $E_f/E_s = 7.2$, one obtains a global buckling mode and the post-buckling behavior appears very unstable, see also (Hutchinson, 2013). In this case, the neo-Hookean model predicts a smaller critical strain. The case of $E_f/E_s = \mathcal{O}(1)$ would deserve additional studies since the patterns are different and therefore are more dependent on boundary conditions and constitutive laws. It has been presented here only for a short comparison with the other cases. In summary, the stiffness ratio E_f/E_s is a crucial parameter to discuss the range of validity of the assumption of a linear elastic substrate. According to our simulations, this assumption seems qualitatively valid for a ratio E_f/E_s larger than 72 but not below.

5. Conclusion

Pattern formation and evolution of thin films attached on rubberlike compliant substrates were investigated from the quantitative standpoint. A fully nonlinear model was developed

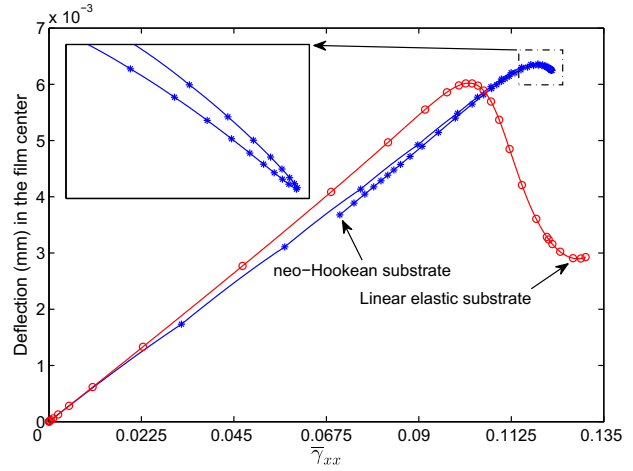

Fig. 16. Comparison of bifurcation curves of soft films with $E_f/E_s = 30$ ($E_f = 54$ MPa, $E_s = 1.8$ MPa) under equi-biaxial compression. Linear elastic model and neo-Hookean hyperelastic model are depicted together. ANM parameters for hyperelastic model: $n = 10, \delta = 10^{-6}$, 60 steps. ANM parameters for linear elastic model: $n = 10, \delta = 10^{-6}$, 65 steps. Each point corresponds to one ANM step.

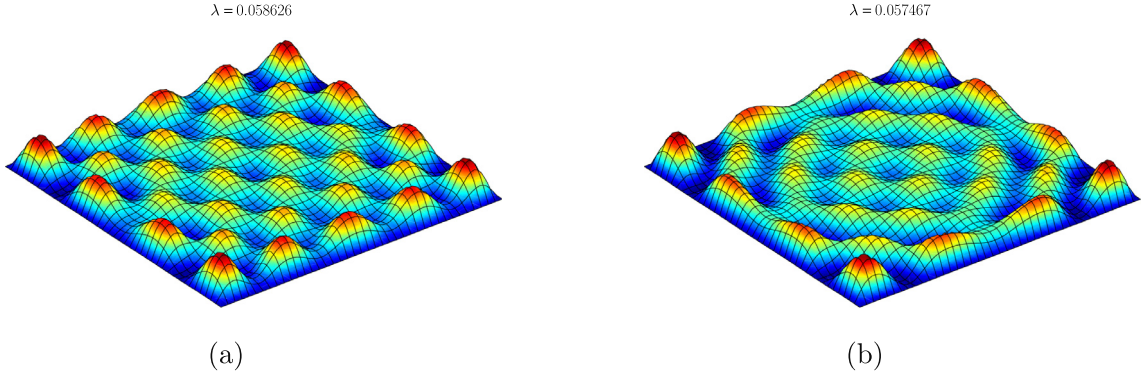

Fig. 14. Film/Sub II with $E_f/E_s = 72$ ($E_f = 130$ MPa, $E_s = 1.8$ MPa) under equi-biaxial compression: (a) final pattern of neo-Hookean hyperelastic model, (b) final pattern of linear elastic model.

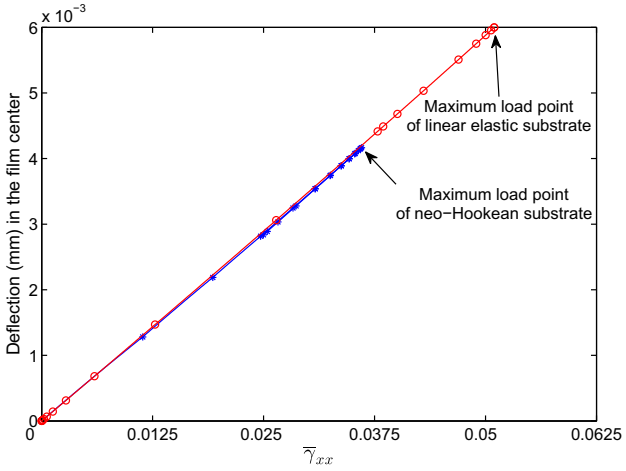

Fig. 17. Comparison of bifurcation curves of soft films with $E_f/E_s = 7.2$ ($E_f = 13$ MPa, $E_s = 1.8$ MPa) under equi-biaxial compression. Linear elastic model and neo-Hookean hyperelastic model are depicted together. ANM parameters for hyperelastic model: $n = 10, \delta = 10^{-6}$, 22 steps. ANM parameters for linear elastic model: $n = 10, \delta = 10^{-6}$, 60 steps. Each point corresponds to one ANM step.

Table 3
Comparison of film/substrate systems modeled with neo-Hookean and linear elastic substrates. The values from linear elastic models are given in parentheses.

E_f/E_s	First bifurcation ($\overline{\gamma}_{xx}$)	Maximum load ($\overline{\gamma}_{xx}$)	neo-Hookean *vs.* linear elasticity
722	1.2% (1.2%)	1.3% (1.4%)	Qualitatively similar
72	2.7% (2.7%)	2.8% (2.9%)	Qualitatively similar
30	12.0% (10.2%)	12.4% (13.2%)	Post-buckling behavior is different
7.2	3.7% (5.1%)	3.7% (5.1%)	Buckling load is different

by associating finite strain hyperelasticity for the substrate and geometrically nonlinear shell formulation for the film. Automatic Differentiation (AD) techniques were applied to improve the ease of the ANM implementation through an operator overloading, which allows one to introduce various potential energy functions of hyperelastic laws in quite a simple and an automatic way. This 3D finite strain model can describe large displacements and large rotations in the film, and finite deformations in the substrate. The occurrence and evolution of fold-like shapes located in sinusoidal and checkerboard patterns have been observed in the post-buckling range. These modes are stable and independent of the loading conditions. Some extremely localized instability modes revealed in the recent literatures, such as folding (Sun et al., 2012) or ridging (Zang et al., 2012) that is obtained from 2D plane strain simulation, have not been found in the present 3D cases.

The comparisons between finite strain hyperelastic models and small strain linear elastic models with respect to different stiffness range of Young's modulus were first discussed. As for a large stiffness ratio, *e.g.* $E_f/E_s \gg \mathcal{O}(10^3)$, the deformation of the system is infinitesimal and the two models are quantitatively equivalent. On the contrary, as for a small stiffness ratio of film/substrate systems, *e.g.* $E_f/E_s \approx \mathcal{O}(10)$, the deformation of the substrate can be large and finite strain models are more appropriate to be taken into account, compared with the linear elastic framework (Xu et al., 2014; Xu et al., 2015).

Acknowledgments

The authors acknowledge the financial support of Fonds National de la Recherche of Luxembourg (Grant No. FNR/C10/MS/784868-WRINKLE). F. Xu and M. Potier-Ferry also acknowledge the financial support of French National Research Agency ANR (Labex DAMAS, Grant No. ANR-11-LABX-0008-01). The authors thank two anonymous reviewers for their helpful comments.

Appendix A. Some operators and notations

According to Nezamabadi et al. (2011), the explicit form of the tensor $\mathbb{H}$ reads

$$\mathbb{H} = (\mathbf{F}_0 \underline{\otimes} \mathbf{I}) : \mathbb{C}_t : \mathbb{B} + \mathbf{I} \underline{\otimes} \mathbf{S}_0, \tag{37}$$

where $\mathbb{B}$ is a fourth order tensor depending on the initial solution $\mathbf{F}_0$ and can be expressed as

$$\mathbb{B} = \frac{1}{2}\left({}^t\mathbf{F}_0 \underline{\otimes} \mathbf{I} + \mathbf{I} \overline{\otimes} \mathbf{F}_0\right). \tag{38}$$

The notations for vector and tensor operations in above equations are defined as

$$\begin{cases} (\mathbf{A} \overline{\otimes} \mathbf{B})_{ijkl} = A_{ik}B_{jl}, \\ (\mathbf{A} \underline{\otimes} \mathbf{B})_{ijkl} = A_{il}B_{jk}, \\ (\mathbf{A} \overline{\underline{\otimes}} \mathbf{B})_{ijkl} = \frac{1}{2}\left(A_{ik}B_{jl} + A_{il}B_{jk}\right). \end{cases} \tag{39}$$

References

Allgower, E.L., Georg, K., 1990. Numerical Continuation Methods. Springer-Verlag, Berlin.
Audoly, B., Boudaoud, A., 2008a. Buckling of a stiff film bound to a compliant substrate–Part I: formulation, linear stability of cylindrical patterns, secondary bifurcations. J. Mech. Phys. Solids 56, 2401–2421.
Audoly, B., Boudaoud, A., 2008b. Buckling of a stiff film bound to a compliant substrate–Part II: a global scenario for the formation of herringbone pattern. J. Mech. Phys. Solids 56, 2422–2443.
Audoly, B., Boudaoud, A., 2008c. Buckling of a stiff film bound to a compliant substrate–Part III: herringbone solutions at large buckling parameter. J. Mech. Phys. Solids 56, 2444–2458.
Baguet, S., Cochelin, B., 2003. On the behaviour of the ANM continuation in the presence of bifurcations. Commun. Numer. Methods Eng. 19, 459–471.
Bischof, C.H., Bücker, H.M., 2000. Computing derivatives of computer programs. In: Grotendorst, J., (Eds.), Modern Methods and Algorithms of Quantum Chemistry: Proceedings, NIC Series, NIC Directors, second ed., vol. 3, pp. 315–327.
Boutyour, E.H., Zahrouni, H., Potier-Ferry, M., Boudi, M., 2004. Bifurcation points and bifurcated branches by an asymptotic numerical method and Padé approximants. Int. J. Numer. Methods Eng. 60, 1987–2012.
Bowden, N., Brittain, S., Evans, A.G., Hutchinson, J.W., Whitesides, G.M., 1998. Spontaneous formation of ordered structures in thin films of metals supported on an elastomeric polymer. Nature 393, 146–149.
Brau, F., Vandeparre, H., Sabbah, A., Poulard, C., Boudaoud, A., Damman, P., 2011. Multiple-length-scale elastic instability mimics parametric resonance of nonlinear oscillators. Nat. Phys. 7, 56–60.
Büchter, N., Ramm, E., Roehl, D., 1994. Three-dimensional extension of non-linear shell formulation based on the enhanced assumed strain concept. Int. J. Numer. Methods Eng. 37, 2551–2568.
Cai, Z., Fu, Y., 1999. On the imperfection sensitivity of a coated elastic half-space. Proc. R. Soc. A 455, 3285–3309.
Cai, Z., Fu, Y., 2000. Exact and asymptotic stability analyses of a coated elastic half-space. Int. J. Solids Struct. 37, 3101–3119.
Cao, Y., Hutchinson, J.W., 2012a. Wrinkling phenomena in neo-Hookean film/substrate bilayers. J. Appl. Mech. 79, 031019-1–031019-9.
Cao, Y., Hutchinson, J.W., 2012b. From wrinkles to creases in elastomers: the instability and imperfection-sensitivity of wrinkling. Proc. R. Soc. A 468, 94–115.
Cao, Y., Jia, F., Zhao, Y., Feng, X., Yu, S., 2012. Buckling and post-buckling of a stiff film resting on an elastic graded substrate. Int. J. Solids Struct. 49, 1656–1664.
Charpentier, I., Potier-Ferry, M., 2008. Automatic differentiation of the asymptotic numerical method: the Diamant approach. C.R Mecanique 336, 336–340.
Chen, X., Hutchinson, J.W., 2004. Herringbone buckling patterns of compressed thin films on compliant substrates. J. Appl. Mech. 71, 597–603.
Cochelin, B., 1994. A path-following technique via an asymptotic-numerical method. Comput. Struct. 53, 1181–1192.
Cochelin, B., Medale, M., 2013. Power series analysis as a major breakthrough to improve the efficiency of asymptotic numerical method in the vicinity of bifurcations. J. Comput. Phys. 236, 594–607.
Cochelin, B., Damil, N., Potier-Ferry, M., 1994. Asymptotic-numerical methods and Padé approximants for non-linear elastic structures. Int. J. Numer. Methods Eng. 37, 1187–1213.

Cochelin, B., Damil, N., Potier-Ferry, M., 2007. Méthode Asymptotique Numérique. Hermès Science Publications.
Cong, Y., Yvonnet, J., Zahrouni, H., 2014. Simulation of instabilities in thin nanostructures by a perturbation approach. Comput. Mech. 53, 739–750.
Damil, N., Potier-Ferry, M., 1990. A new method to compute perturbed bifurcation: application to the buckling of imperfect elastic structures. Int. J. Eng. Sci. 26, 943–957.
Damil, N., Potier-Ferry, M., 2010. Influence of local wrinkling on membrane behaviour: a new approach by the technique of slowly variable Fourier coefficients. J. Mech. Phys. Solids 58, 1139–1153.
Doedel, E., 1981. AUTO: a program for the automatic bifurcation analysis of autonomous systems. Congr. Numer. 30, 265–284.
Dowaikh, M.A., Ogden, R.W., 1990. On surface waves and deformations in a pre-stressed incompressible elastic solid. IMA J. Appl. Math. 44, 261–284.
Efimenko, K., Rackaitis, M., Manias, E., Vaziri, A., Mahadevan, L., Genzer, J., 2005. Nested self-similar wrinkling patterns in skins. Nat. Mater. 4, 293–297.
Forth, S.A., Edvall, M.M., 2007. User Guide for Mad–a Matlab Automatic Differentiation Toolbox, TOMLAB/MAD, version 1.4.
Gent, A.N., 1996. A new constitutive relation for rubber. Rubber. Chem. Technol. 69, 59–61.
Griewank, A., 2000. Evaluating derivatives: principles and techniques of algorithmic differentiation. Front. Appl. Math. 19, SIAM, Philadelphia.
Hayes, M.A., Rivlin, R.S., 1961. Surface waves in deformed elastic materials. Arch. Ration. Mech. Anal. 8, 358–380.
Holzapfel, G.A., 2000. Nonlinear Solid Mechanics: A Continuum Approach for Engineering. Wiley, Chichester, England.
Huang, R., Im, S., 2006. Dynamics of wrinkle growth and coarsening in stressed thin films. Phys. Rev. E 74, 026214-1–026214-12.
Huang, Z.Y., Hong, W., Suo, Z., 2004. Evolution of wrinkles in hard films on soft substrates. Phys. Rev. E 70, 030601-1–030601-4.
Huang, Z.Y., Hong, W., Suo, Z., 2005. Nonlinear analyses of wrinkles in a film bonded to a compliant substrate. J. Mech. Phys. Solids 53, 2101–2118.
Hutchinson, J.W., 2013. The role of nonlinear substrate elasticity in the wrinkling of thin films. Phil. Trans. R. Soc. A 371, 20120422.
Koutsawa, Y., Charpentier, I., Daya, E.M., Cherkaoui, M., 2008. A generic approach for the solution of nonlinear residual equations. Part I: the Diamant toolbox. Comput. Methods Appl. Mech. Eng. 198, 572–577.
Lejeune, A., Béchet, F., Boudaoud, H., Mathieu, N., Potier-Ferry, M., 2012. Object-oriented design to automate a high order non-linear solver based on asymptotic numerical method. Adv. Eng. Softw. 48, 70–88.
Lejeune, A., Boudaoud, H., Potier-Ferry, M., Charpentier, I., Zahrouni, H., 2013. Automatic solver for non-linear partial differential equations with implicit local laws: application to unilateral contact. Int. J. Numer. Methods Eng. 94, 850–867.
Li, B., Jia, F., Cao, Y.P., Feng, X.Q., Gao, H., 2011. Surface wrinkling patterns on a core-shell soft sphere. Phys. Rev. Lett. 106, 234301-1–234301-4.
Medale, M., Cochelin, B., 2009. A parallel computer implementation of the asymptotic numerical method to study thermal convection instabilities. J. Comput. Phys. 228, 8249–8262.
Nezamabadi, S., Zahrouni, H., Yvonnet, J., 2011. Solving hyperelastic material problems by asymptotic numerical method. Comput. Mech. 47, 77–92.
Ogden, R.W., 1984. Non-linear Elastic Deformations. Ellis Horwood, Chichester, England.
Rogers, J.A., Someya, T., Huang, Y., 2010. Materials and mechanics for stretchable electronics. Science 327, 1603–1607.
Shield, T.W., Kim, K.S., Shield, R.T., 1994. The buckling of an elastic layer bonded to an elastic substrate in plane strain. J. Appl. Mech. 61, 231–235.
Simo, J.C., Rifai, M.S., 1990. A class of mixed assumed strain methods and method of incompatible modes. Int. J. Numer. Methods Eng. 37, 1595–1636.
Song, J., Jiang, H., Liu, Z.J., Khang, D.Y., Huang, Y., Rogers, J.A., Lu, C., Koh, C.G., 2008. Buckling of a stiff thin film on a compliant substrate in large deformation. Int. J. Solids Struct. 45, 3107–3121.
Steigmann, D., Ogden, R.W., 1997. Plane deformations of elastic solids with intrinsic boundary elasticity. Proc. R. Soc. A 453, 853–877.
Stoop, N., Lagrange, R., Terwagne, D., Reis, P.M., Dunkel, J., 2015. Curvature-induced symmetry breaking determines elastic surface patterns. Nat. Mater. 14, 337–342.
Sun, J.Y., Xia, S., Moon, M.W., Oh, K.H., Kim, K.S., 2012. Folding wrinkles of a thin stiff layer on a soft substrate. Proc. R. Soc. A 468, 932–953.
Vannucci, P., Cochelin, B., Damil, N., Potier-Ferry, M., 1998. An asymptotic-numerical method to compute bifurcating branches. Int. J. Numer. Methods Eng. 41, 1365–1389.
Walther, A., Griewank, A., 2010. ADOL-C: A package for the automatic differentiation of algorithms written in C/C++, version 2.1.12-stable.
Wang, S., Song, J., Kim, D.H., Huang, Y., Rogers, J.A., 2008. Local versus global buckling of thin films on elastomeric substrates. Appl. Phys. Lett. 93, 023126-1–023126-3.
Xu, F., 2014. Numerical study of instability patterns of film-substrate systems (Ph.D. thesis), Université de Lorraine, France.
Xu, F., Potier-Ferry, M., Belouettar, S., Cong, Y., 2014. 3D finite element modeling for instabilities in thin films on soft substrates. Int. J. Solids Struct. 51, 3619–3632.
Xu, F., Potier-Ferry, M., Belouettar, S., Hu, H., 2015. Multiple bifurcations in wrinkling analysis of thin films on compliant substrates. Int. J. Nonlinear Mech. http://dx.doi.org/10.1016/j.ijnonlinmec.2014.12.006.
Yin, J., Yagüe, J.L., Eggenspieler, D., Gleason, K.K., Boyce, M.C., 2012. Deterministic order in surface micro-topologies through sequential wrinkling. Adv. Mater. 24, 5441–5446.
Zahrouni, H., Cochelin, B., Potier-Ferry, M., 1999. Computing finite rotations of shells by an asymptotic-numerical method. Comput. Methods Appl. Mech. Eng. 175, 71–85.
Zang, J., Zhao, X., Cao, Y., Hutchinson, J.W., 2012. Localized ridge wrinkling of stiff films on compliant substrates. J. Mech. Phys. Solids 60, 1265–1279.